Inorg. Chem. **2006**, *45*, 8533–8542

Density Functional Theory Study of Fe(IV) d–d Optical Transitions in Active-Site Models of Class I Ribonucleotide Reductase Intermediate X with Vertical Self-Consistent Reaction Field Methods

Wen-Ge Han,* Tiqing Liu,[†] Timothy Lovell,[‡] and Louis Noodleman*

Department of Molecular Biology, TPC15, The Scripps Research Institute, 10550 N. Torrey Pines Road, La Jolla, California 92037

Received April 4, 2006

The Fe(IV) d–d transition energies for four active-site structural models of class I ribonucleotide reductase (RNR) intermediate X have been calculated using broken-symmetry density functional theory incorporated with the Slater transition state vertical self-consistent reaction field methodology. Our model I (Figure 1), which contains two μ-oxo bridges, one terminal water, and one bidentate carboxylate group, yields the best Fe(IV) d–d transition energies compared with experiment. Our previous study (*J. Am. Chem. Soc.* **2005**, *127*, 15778–15790) also shows that most of the other calculated properties of model I in both native and mutant Y122F forms, including geometries, spin states, pK_a's, ^{57}Fe, ^{1}H, and ^{17}O hyperfine tensors, and ^{57}Fe Mössbauer isomer shifts and quadrupole splittings, are also the best in agreement with the available experimental data. This model is likely to represent the active-site structure of the intermediate state X of RNR.

1. Introduction

The intermediate X of class I ribonucleotide reductase (RNR) is the required state to oxidize a tyrosine (Tyr 122 in *Escherichia coli*) in RNR subunit R2 to a stable radical form.[1−5] This radical functions as a "pilot light", which begins the catalytic reaction by a long-range proton-coupled electron-transfer process to generate a thiyl radical on cysteine 439 in RNR subunit R1, which then performs the reduction of ribonucleotides to 2′-deoxyribonucleotides, the precursors required in the initial step in DNA biosynthesis.[6−11]

Many experimental and theoretical efforts have been made in order to investigate the detailed structure, oxidation, and spin state of RNR-X.[12−23] Many of these studies have been reviewed in ref 20. The combination of Q-band ENDOR (electron−nuclear double resonance) and the best-fit Mössbauer isomer shift and quadrupole splitting data on mutant

* To whom correspondence should be addressed. E-mail: wengehan@scripps.edu (W.-G.H.), lou@scripps.edu (L.N.). Fax: 858-7848896.

[†] Present address: University of Maryland Biotechnology Institute, Center for Advanced, Research in Biotechnology, 9600 Gudelsky Drive, Rockville, MD 20850.

[‡] Present address: AstraZeneca R and D Molndal, SE-431 83 Molndal, Sweden.

(1) Bollinger, J. M.; Edmondson, D. E.; Huynh, B. H.; Filley, J.; Norton, J. R.; Stubbe, J. *Science* **1991**, *253*, 292−298.
(2) Bollinger, J. M., Jr.; Stubbe, J.; Huynh, B. H.; Edmondson, D. E. *J. Am. Chem. Soc.* **1991**, *113*, 6289−6291.
(3) Bollinger, J. M., Jr.; Tong, W. H.; Ravi, N.; Huynh, B. H.; Edmondson, D. E.; Stubbe, J. In *Methods in Enzymology*; Klinman, J. P., Ed.; Academic Press: New York, 1995; p 258.
(4) Ravi, N.; Bollinger, J. M., Jr.; Huynh, B. H.; Edmondson, D. E.; Stubbe, J. *J. Am. Chem. Soc.* **1994**, *116*, 8007−8014.
(5) Ravi, N.; Bominaar, E. L. *Inorg. Chem.* **1995**, *34*, 1040−1043.
(6) Fontecave, M.; Nordlund, P.; Eklund, H.; Reichard, P. *Adv. Enzymol. Relat. Areas Mol. Biol.* **1992**, *65*, 147−183.
(7) Fontecave, M. *Cell Mol. Life Sci.* **1998**, *54*, 684−695.
(8) Wallar, B. J.; Lipscomb, J. D. *Chem. Rev.* **1996**, *96*, 2625−2658.
(9) Sjoberg, B. M. *Struct. Bonding* **1997**, *88*, 139−173.
(10) Stubbe, J.; van der Donk, W. A. *Chem. Rev.* **1998**, *98*, 705−762.
(11) Bennati, M.; Lendzian, F.; Schmittel, M.; Zipse, H. *Biol. Chem.* **2005**, *386*, 1007−1022.
(12) Sturgeon, B. E.; Burdi, D.; Chen, S.; Huynh, B.-H.; Edmondson, D. E.; Stubbe, J.; Hoffman, B. M. *J. Am. Chem. Soc.* **1996**, *118*, 7551−7557.
(13) Riggs-Gelasco, P. J.; Shu, L.; Chen, S.; Burdi, D.; Huynh, B. H.; Que, L., Jr.; Stubbe, J. *J. Am. Chem. Soc.* **1998**, *120*, 849−860.
(14) Willems, J.-P.; Lee, H.-I.; Burdi, D.; Doan, P. E.; Stubbe, J.; Hoffman, B. M. *J. Am. Chem. Soc.* **1997**, *119*, 9816−9824.
(15) Burdi, D.; Willems, J.-P.; Riggs-Gelasco, P.; Antholine, W. E.; Stubbe, J.; Hoffman, B. M. *J. Am. Chem. Soc.* **1998**, *120*, 12910−12919.
(16) Mitić, N.; Saleh, L.; Schenk, G.; Bollinger, J. M. J.; Solomon, E. I. *J. Am. Chem. Soc.* **2003**, *125*, 11200−11201.
(17) Han, W.-G.; Lovell, T.; Liu, T.; Noodleman, L. *Inorg. Chem.* **2003**, *42*, 2751−2758.
(18) Han, W.-G.; Lovell, T.; Liu, T.; Noodleman, L. *Inorg. Chem.* **2004**, *43*, 613−621.
(19) Han, W.-G.; Liu, T.; Lovell, T.; Noodleman, L. *J. Am. Chem. Soc.* **2005**, *127*, 15778−15790.
(20) Han, W.-G.; Liu, T.; Lovell, T.; Noodleman, L. *J. Inorg. Biochem.* **2006**, *100*, 771−779.
(21) Siegbahn, P. E. M. *Inorg. Chem.* **1999**, *38*, 2880−2889.
(22) Siegbahn, P. E. M. *Chem. Phys. Lett.* **2002**, *351*, 311−318.
(23) Siegbahn, E. M. *Q. Rev. Biophys.* **2003**, *36*, 91−145.

10.1021/ic060566+ CCC: $33.50
Published on Web 09/14/2006

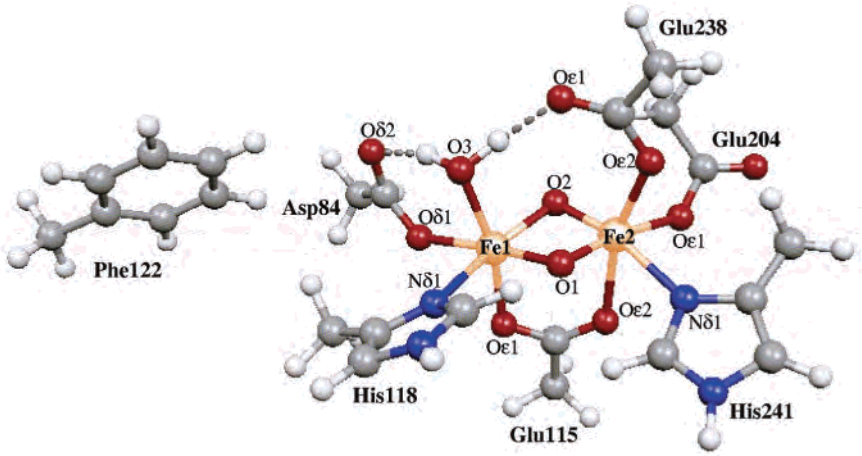

Figure 1. Active-site model for RNR-X. Model I is in Y122F form. The corresponding model in native form was shown in Figure 4 of ref 19. The figure is generated with *MOLEKEL*[24] and Xfig.[25]

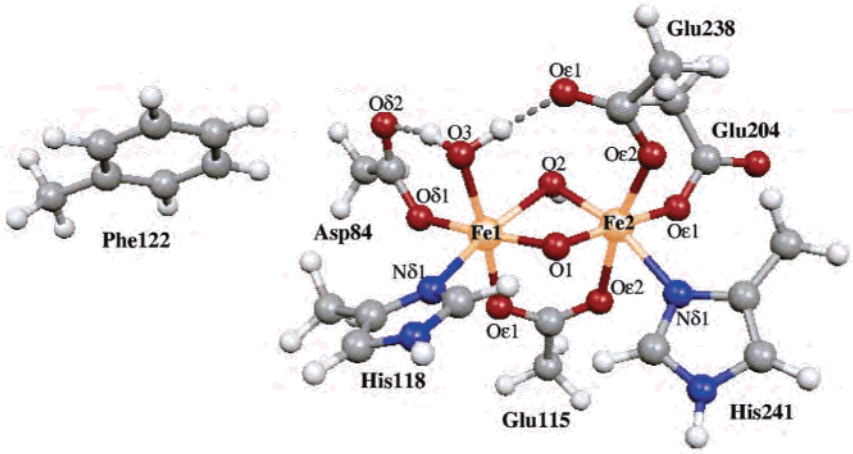

Figure 2. Y122F form model II for the active-site structure of RNR-X. The corresponding wild-type model can be found in Figure 5 of ref 19.

Y122F-R2 indicates that the iron centers of X are high-spin Fe(III) ($S = {}^5/_2$) and high-spin Fe(IV) ($S = 2$) sites that antiferromagnetically (AF) couple to give an $S_{total} = {}^1/_2$ ground state.[12] In the past years, our group has started a series of theoretical studies of proposed RNR-X type species using broken-symmetry density functional theory (DFT) and spin-projection methods. The results have been presented in three publications.[17−19] In our latest study,[19] the properties of three new models (models I−III in both native and Y122F mutant forms) and one previously studied model (X_{2nd}) were calculated and compared with available experimental data. These properties include geometries, spin states, pK_a's, ^{57}-Fe, ^{1}H, and ^{17}O hyperfine tensors, ^{57}Fe Mössbauer isomer shifts and quadrupole splittings, and Fe(IV) d−d transition energies. On the basis of detailed analysis and comparisons, we found that model I, a bis(μ-oxo)-bridged AF-coupled Fe1(III)−Fe2(IV) state (Fe1 is the iron site closer to Tyr122, and both Fe1 and Fe2 are high spin) is the best of all models tested[17−19] in reproducing the important observed properties of RNR-X.

The native forms (containing Tyr122) of models I−III can be found in Figures 4−6 in ref 19. Their mutant Y122F forms are shown in Figures 1−3, respectively. The large cluster X_{2nd} was given in Figure 2 of ref 18, and its core structure in Y122F form, which is studied in the current paper, is shown in Figure 4. X_{2nd} was originally constructed following the proposal by Burdi et al.[15] that X may contain two oxygen atoms, with one present as a μ-oxo bridge and one as a terminal aqua ligand bound to the Fe(III) site, and one or two additional mono-oxygen bridges provided by the carboxylate oxygens of Glu115 and Glu238.

Recently, Mitić et al. performed rapid-freeze-quench magnetic circular dichroism (MCD) measurements on X in the double mutant Y122F/Y356F RNR-R2.[16] Three low-energy bands at 16 700, 19 400, and 22 100 cm^{-1} (or 2.07, 2.41, and 2.74 eV) were assigned as the lowest spin-allowed ligand-field d−d transitions of an Fe(IV) site. In our latest study,[19] we have also estimated the Fe(IV) d−d transition energies for models I−III (Y122F forms) and the large cluster of X_{2nd}, which are all in the high-spin AF-coupled Fe1(III)−Fe2(IV) state, by comparing the ground-state molecular orbital energy differences between the occupied and virtual orbitals that contain significant Fe2(IV) d populations. To evaluate the Fe(IV) d−d transition energies more accurately,

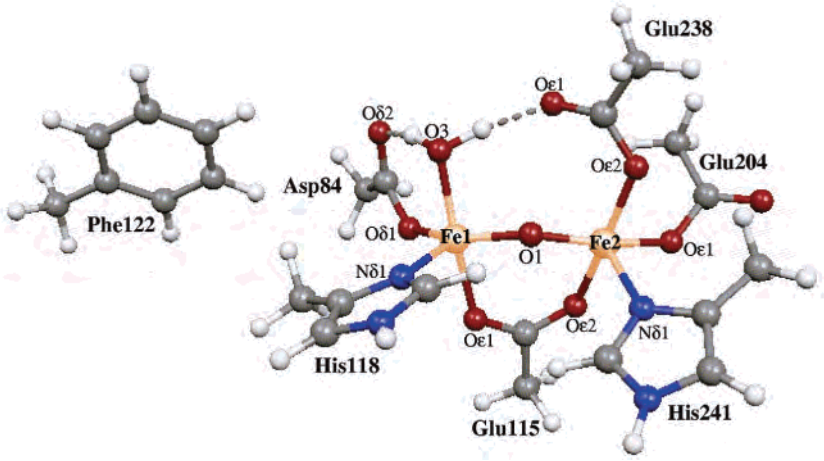

Figure 3. Y122F form model III for the active-site structure of RNR-X. Model III in native form was shown in Figure 6 of ref 19.

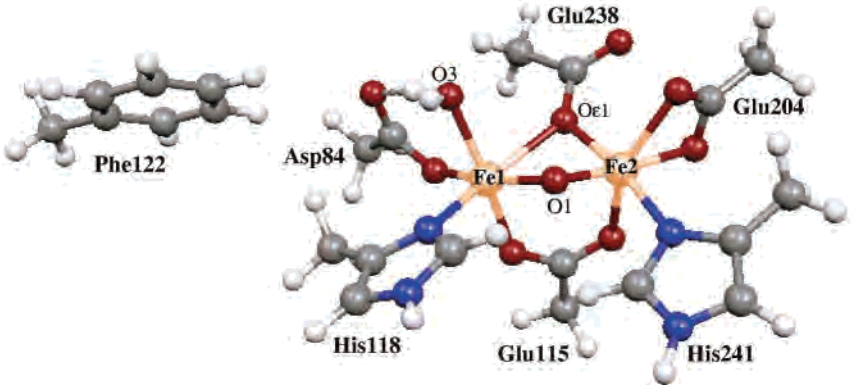

Figure 4. First-shell model of X_{2nd} in Y122F form. The larger wild-type models containing some second- and third-shell hydrogen-bonding residue side chains have been studied in refs 18 and 19.

we have now performed Slater transition state vertical self-consistent reaction field (STS-VSCRF) calculations on these model clusters. For equivalent comparison with models I−III, we reduced X_{2nd} to the same size as models I−III. All four models calculated here are in Y122F forms (Figures 1−4).

The STS method has been widely used to calculate the one-electron excitation energies within DFT.[26−29] In this method, half an electron is promoted from an occupied molecular orbital to an unoccupied molecular orbital. The excitation energy of the actual one-electron transition between these two orbitals can be well approximated by the energy (orbital eigenvalue) difference of these two half-occupied orbitals in the STS.[27,29−31] It is well-known that the STS is an excellent approximation to the corresponding ΔSCF excitation energy for a one-electron excitation. The ΔSCF method includes electron relaxation of the passive orbitals and has given good results for d → d and charge-transfer transitions in spin-polarized and spin-coupled systems. In addition, the STS exhibits better stability and convergence than direct ΔSCF hole states.

Very recently, we have established a DFT VSCRF solvation model for predicting vertical excitation energies of solutes in solvents with different polarities and have applied this methodology to predict both the excitation and emission energies of solvent-sensitive dyes in different solvents.[32,33] According to the Franck−Condon principle,[34] the electronic transition during optical absorption is a vertical excitation, in which only the electronic relaxation of both the solute and solvent molecules will occur, while the positions of the nuclei in the whole system will remain unchanged. After the excitation, the solute and solvent molecules will normally reorient, and a new solvation equilibrium in the excited state will be established. Emission

(24) Flükiger, P.; Lüthi, H. P.; Portmann, S.; Weber, J. *MOLEKEL 4.0*; Swiss Center for Scientific Computing: Manno, Switzerland, 2000.
(25) Xfig 3.2.4, Copyright 1985−1988 by SupojSutanthavibul; Parts Copyright 1989−1998 by Brian V. Smith; Parts Copyright 1991 by Paul King.
(26) Slater, J. C. In *Advances in Quantum Chemistry*; Löwdin, P.-O., Ed.; Academic Press, Inc.: New York, 1972; Vol. 6, pp 1−92.
(27) Slater, J. C. *The Self-Consistent Field for Molecules and Solids: Quantum Theory of Molecules and Solids*; McGraw Hill: New York, 1974.
(28) Wood, J. H. *Chem. Phys. Lett.* **1977**, *51*, 582−584.
(29) Noodleman, L.; Baerends, E. J. *J. Am. Chem. Soc.* **1984**, *106*, 2316−2327.
(30) Tanaka, I.; Adachi, H. *Phys. Rev. B* **1996**, *54*, 4604−4608.
(31) Liberman, D. A. *Phys. Rev. B* **2000**, *62*, 6851−6853.
(32) Han, W.-G.; Liu, T.; Himo, F.; Toutchkine, A.; Bashford, D.; Hahn, K. M.; Noodleman, L. *ChemPhysChem* **2003**, *4*, 1084−1094.
(33) Liu, T.; Han, W.-G.; Himo, F.; Ullmann, G. M.; Bashford, D.; Toutchkine, A.; Hahn, K. M.; Noodleman, L. *J. Phys. Chem. A* **2004**, *108*, 3545−3555.
(34) Turro, N. J. *Modern Molecular Photochemistry*; University Science Books: Mill Valley, CA, 1991.

or fluorescence will happen from this equilibrium state, which is also a vertical electronic transition process.

Our VSCRF model was developed in the framework of DFT with ΔSCF methodology. Its implementation is based on our original self-consistent reaction field (SCRF) development,[35−38] where the solute molecule is computed by DFT in the presence of a solvent reaction field. The reaction field is evaluated from a finite-difference solution to the Poisson−Boltzmann equation, and self-consistency between the reaction field and the electronic structure of the solute is achieved by iteration. The SCRF calculations applied to solute geometry allow electronic structure relaxation in both the solute and solvent and, implicitly, the orientational (geometry) relaxation of the solvent. Once the SCRF calculation on the ground state is achieved, the VSCRF procedure on the excited state allows only the electronic structure reorganization for both the solute and solvent, and the vertical excitation in solution is then obtained.

The details of the VSCRF method have been given in ref 33. The active-site models, and the energetic and geometry optimization calculations have been described in ref 19. Here we will briefly describe the theoretical framework and calculational steps to obtain the vertical Fe(IV) d−d transition energies. The calculated results for models I−III and X_{2nd} (Y122F) will then be presented.

2. Methodology

All DFT spin-unrestricted broken-symmetry[19] calculations have been performed using the Amsterdam Density Functional (ADF) package.[19,39,40] The geometries of Y122F type models I−III in the AF-coupled Fe1(III)−Fe2(IV) state with high-spin sites have been optimized within the COSMO (conductor-like screening model) solvation model with dielectric constant $\epsilon = 80.0$ in ref 19, using VWN(local)−PW91(nonlocal) potential,[41,42] and using the triple-ζ plus polarization (TZP) basis set for the two iron sites and double-ζ plus polarization (DZP) basis set for other atoms with the inner-core shells of C(1s), N(1s), O(1s), and Fe(1s,2s,2p) frozen. The COSMO model is a dielectric solvent continuum model in which the solute molecule is embedded in a molecular-shaped cavity surrounded by a dielectric medium with a given dielectric constant.[43−45] Similarly, the geometry of the high-spin AF-coupled Fe1(III)−Fe2(IV) state X_{2nd} (Y122F) in Figure 4 was also optimized in the current study. The Fe1−Fe2 distance in this COSMO-optimized X_{2nd} structure is 2.933 Å, which is much longer than that in model I (2.703 Å for Y122F form; see Table S3 in the Supporting Information in ref 19). The Cartesian coordinates of the optimized geometries of models I−III and X_{2nd} (Y122F) are given in the Supporting Information.

To calculate the Fe2(IV) d−d transition energies, our current SCRF/VSCRF calculations are performed at the COSMO-optimized ground-state geometries of the model clusters using TZP basis sets for all atom types without freezing any core electrons.

If an electron is excited from orbital n_i in the ground state (initial state, i) to orbital n_j in the excited state (final state, f), the excitation energy ΔE will be

$$\Delta E = E_f - E_i \quad (1)$$

where E_i is the energy (including the solvation energy) of the system in the ground state and E_f is the energy in the vertical excited state. In our previous studies on solvent-sensitive dyes, we used eq 1 (also see eq 3 below) to calculate the vertical excitation energies of the dye molecules from the ground state to the first excited singlet state in different solvents.[32,33] E_i was obtained by a normal SCRF calculation at the COSMO-optimized ground-state molecular geometry, and E_f was obtained from VSCRF calculation.

For the current Fe2(IV) d−d transition calculations, we promote a β (the majority spin of Fe2) electron from an occupied molecular orbital to an unoccupied molecular orbital and see if this generates a unique Fe2(IV) d−d transition according to the Fe2(IV) d populations of these two orbitals in the final vertical excited state. The occupied molecular orbitals we studied are from $n_H - p$ (p is up to 17 in our current study) to n_H [n_H represents the highest occupied molecular orbital (HOMO)]. The unoccupied molecular orbitals involved in the Fe2(IV) d−d transitions are n_L, $n_L + 1$, $n_L + 3$, and $n_L + 4$ [n_L is the lowest unoccupied molecular orbital (LUMO)]. We find that the difficulty in excited-state SCF convergence is a major problem for most of these one-electron excitation calculations because of the oscillation of the energy levels with changes in occupation numbers.[46] Only three Fe2(IV) d−d transition VSCRF calculations were converged for model I (Y122F) among all one-electron excitation VSCRF calculations of the four models. On the other hand, the SCF convergence is relatively easier to reach in the STS-VSCRF calculations. Because only half an electron is promoted from the occupied orbital n_i to the unoccupied orbital n_j, the oscillation of the energy levels during SCF is smoothed.[29,46] We therefore have performed the STS-VSCRF calculations to obtain a complete set of the

(35) Chen, J. L.; Noodleman, L.; Case, D. A.; Bashford, D. *J. Phys. Chem.* **1994**, *98*, 11059−11068.
(36) Bashford, D. In *Scientific Computing in Object-Oriented Parallel Environments (Lecture Notes in Computer Science)*; Ishikawa, Y., Oldehoeft, R. R., Reynders, J. V. W., Tholburn, M., Eds.; Springer: Berlin, 1997; Vol. 1343, pp 233−240.
(37) Li, J.; Fisher, C. L.; Chen, J. L.; Bashford, D.; Noodleman, L. *Inorg. Chem.* **1996**, *35*, 4694−4702.
(38) Li, J.; Nelson, M. R.; Peng, C. Y.; Bashford, D.; Noodleman, L. *J. Phys. Chem. A* **1998**, *102*, 6311−6324.
(39) te Velde, G.; Bickelhaupt, F. M.; Baerends, E. J.; Guerra, C. F.; Van Gisbergen, S. J. A.; Snijders, J. G.; Ziegler, T. *J. Comput. Chem.* **2001**, *22*, 931−967.
(40) Guerra, C. F.; Snijders, J. G.; te Velde, G.; Baerends, E. J. *Theor. Chem. Acc.* **1998**, *99*, 391−403.
(41) Vosko, S. H.; Wilk, L.; Nusair, M. *Can. J. Phys.* **1980**, *58*, 1200−1211.
(42) Perdew, J. P.; Chevary, J. A.; Vosko, S. H.; Jackson, K. A.; Pederson, M. R.; Singh, D. J.; Fiolhais, C. *Phys. Rev. B* **1992**, *46*, 6671−6687.
(43) Klamt, A.; Schüürmann, G. *J. Chem. Soc., Perkin Trans. 2* **1993**, 799−805.
(44) Klamt, A. *J. Phys. Chem.* **1995**, *99*, 2224−2235.
(45) Klamt, A.; Jonas, V. *J. Chem. Phys.* **1996**, *105*, 9972−9981.
(46) Noodleman, L.; Lovell, T.; Han, W.-G.; Li, J.; Himo, F. *Chem. Rev.* **2004**, *104*, 459−508.

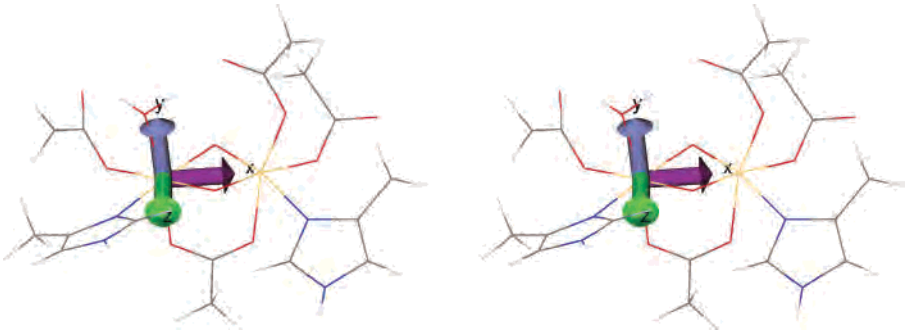

Figure 5. Stereo picture of the diiron center of model I (Y122F) with *xyz* axes. The figure is generated with VMD.[48]

Table 1. Fe(IV) d−d $n_i \rightarrow n_j = n_L + 3$ Transition Energies (ΔE_{VSCRF}) (eV) and Fe(IV) d Orbital Populations (%) Obtained from Normal VSCRF Calculations (Equation 3) for Model I (Y122F) in a High-Spin AF-Coupled Fe1(III)−Fe2(IV) State[a]

	$n_i \rightarrow n_L + 3$	Fe(IV) d populations	
n_i	ΔE_{VSCRF}	n_i	$n_L + 3$
n_H	1.95	$d_{x^2-y^2}$ (17.2), d_{z^2} (11.3), d_{xy} (9.1)	d_{xz} (41.5), d_{yz} (2.4)
$n_H - 1$	2.53	d_{yz} (12.4), d_{xz} (1.4)	d_{xz} (40.0), d_{yz} (2.0)
$n_H - 2$	2.56	d_{yz} (13.4), d_{xz} (1.2)	d_{xz} (40.0), d_{yz} (2.0)

[a] n_H and n_L represent the position of the β spin [the majority spin on the Fe(IV) site] HOMO and LUMO, respectively. Only the virtual orbital $n_L + 3$ contains significant Fe(IV) d characteristics for model I (Y122F). Populations correspond to the vertical excited state containing the valence hole.

Fe2(IV) d−d transition energies for this study. The excitation energy ΔE_{ij} is then approximated as the difference $\Delta\epsilon_{ij}$(STS) of the orbital eigenvalues ϵ_j and ϵ_i in the converged STS-VSCRF calculation:

$$\Delta E \approx \Delta\epsilon_{ij}(\mathrm{STS}) = \epsilon_j - \epsilon_i \qquad (2)$$

To obtain the ground-state reaction field potential for the VSCRF calculations, one needs to perform the normal SCRF on the COSMO-optimized geometries of the RNR-X active-site models. The SCRF procedure is described briefly as follows: (1) One performs a gas-phase single-point energy calculation on the COSMO-optimized model structure. (2) The CHELPG program[35] is then used to fit the point charges of each atom from the molecular electrostatic potentials (ESPs) calculated by ADF. (3) One performs the solvation calculation by using the MEAD (Macroscopic Electrostatics with Atomic Detail) program developed by Bashford,[36,47] to solve the Poisson−Boltzmann equation with a numerical finite-difference method. $\epsilon = 1$ and 80 are used inside and outside the model cluster region, respectively. (4) One adds the reaction field potential obtained from step 3 to the Hamiltonian of the ADF single-point energy calculation. The iteration of steps 1−4 continues until self-consistency between the reaction field potential and the electronic structure of the active-site model is achieved.

In the end of the SCRF iteration, the electronic density distribution and the potential resulting from the reaction field and the ESP charges at the nuclei are then saved for VSCRF calculation. For the normal one-electron excitation VSCRF calculations, the optical absorption (E_{abs}) energy can be described as[33]

$$E_{abs} = \Delta E = E_f - E_i = E_0^f - E_0^i + \frac{1}{2}\{\int[2\phi_{i,eq}^{(r)}(x) + \Delta\phi_{op}^{(r)}(x)]\Delta\rho_{if}(x)\, d^3x\}$$
$$= \Delta E_0 + \Delta G_{pot} + \Delta G_{res} \qquad (3)$$

where E_0^i and E_0^f are the electronic energies of the model cluster at the initial (ground-state) and final (excited-state) charge distributions, respectively; $\phi_{i,eq}^{(r)}$ is the reaction potential of ρ_i obtained from Poisson solutions for the initial ground state with dielectric constant $\epsilon = 1.0$ in the solute region and the ϵ_{eq} (here $\epsilon_{eq} = 80.0$ for water) in the solvent region (outside the solute cavity). During the vertical electronic transition, the dielectric constant $\epsilon_{op} \approx 2.0$ is set to the solvent region, which corresponds to the relaxation of the solvent electronic distribution. And $\Delta\phi_{op}^{(r)}$ is the reaction potential of $\Delta\rho_{if}$ obtained from Poisson solutions with the outside dielectric set to ϵ_{op}. The vertical transition energy is described by the sum of three terms: (1) $\Delta E_0 = E_0^f - E_0^i$ is the change in the solute electronic energy upon one-electron excitation; (2) the potential term $\Delta G_{pot} = \int\phi_{i,eq}^{(r)}\Delta\rho_{if}(x)\, d^3x$, which describes the change of the reaction field energy caused by the reorganization of the solute electronic structure; and (3) the response term $\Delta G_{res} = {}^1/_2\{\int\Delta\phi_{op}^{(r)}(x)\ \Delta\rho_{if}(x)\ d^3x\ \}$, which is the change of the free energy due to the electronic relaxation in the solvent.

The iterative procedure in VSCRF can be described as follows: (1) The normal one-electron excited or STS single-point energy calculation is performed at the ground-state COSMO-optimized geometry. The reaction field potential ($\phi_i^r = \phi_{i,eq}^{(r)}$) of the solvated relaxed ground state (obtained from converged SCRF) is added to the Hamiltonian of this calculation. (2) The electronic density distribution (ρ_f) is taken from step 1, and the ESP charges are fitted. (3) The differences of electronic densities ($\Delta\rho_{if}$'s) between the current excited state (or STS) and the relaxed ground state over the grids of the ADF program are computed. (4) A set of the ESP charge differences for each atom center between the current state and the relaxed state is also calculated. Using this set of ESP difference charges (again with $\epsilon = 1$ in solute region), we then perform a MEAD calculation to get the

(47) Bashford, D.; Gerwert, K. *J. Mol. Biol.* **1992**, *224*, 473−486.
(48) Humphrey, W.; Dalke, A.; Schulten, K. *J. Mol. Graphics* **1996**, *14*, 33−38.

Table 2. Fe(IV) d−d $n_i \rightarrow n_j = n_L + 3$ Excitation Energies (Calculated $\Delta\epsilon_{STS-VSCRF}$ from Equation 2 and Experimental ΔE_{exp}) (eV), Band Numbers, and Fe(IV) d Orbital Populations (%) Obtained from STS-VSCRF Calculations for Model I (Y122F) in a High-Spin AF-Coupled Fe1(III)−Fe2(IV) State

		transition energy		Fe(IV) d populations	
band	n_i	$\Delta\epsilon_{STS-VSCRF}$	ΔE_{exp} [a]	n_i	$n_L + 3$
1	n_H	1.95	2.07	$d_{x^2-y^2}$ (16.8), d_{z^2} (9.7), d_{xy} (8.3)	d_{xz} (41.1), d_{yz} (2.2)
2	$n_H - 1$	2.54	2.41	d_{yz} (10.4), d_{xz} (1.2)	d_{xz} (40.2), d_{yz} (2.0)
	$n_H - 2$	2.57		d_{yz} (11.6), d_{xz} (1.0)	d_{xz} (40.1), d_{yz} (2.0)
3	$n_H - 3$	2.89	2.74	d_{z^2} (7.5), $d_{x^2-y^2}$ (3.8)	d_{xz} (40.0), d_{yz} (2.0)
4	$n_H - 4$	2.71		d_{yz} (8.6), d_{xy} (1.2), $d_{x^2-y^2}$ (1.8)	d_{xz} (40.7), d_{yz} (2.0)
	$n_H - 5$	3.23		d_{yz} (1.8)	d_{xz} (40.1), d_{yz} (2.1)

[a] The experimental data are taken from ref 16.

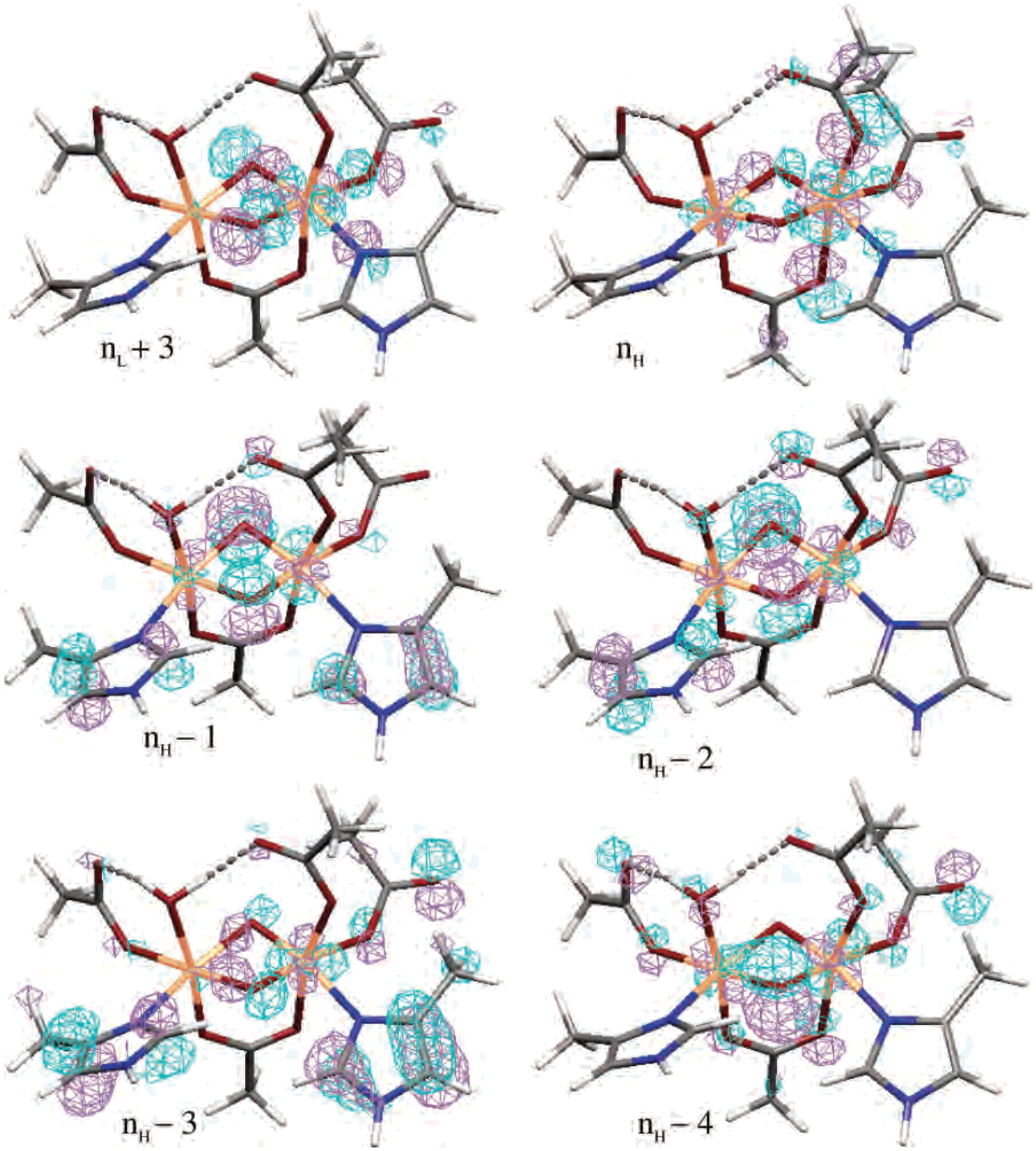

Figure 6. Molecular orbital plots for the half-electrons in the vertical STSs of model I (Y122F). Orbitals $n_L + 3$ and n_H are taken from the $n_H \rightarrow n_L + 3$ STS-VSCRF calculation, and orbitals $n_H - 1$, $n_H - 2$, $n_H - 3$, and $n_H - 4$ are taken from the corresponding $n_H - 1$, $n_H - 2$, $n_H - 3$, $n_H - 4 \rightarrow n_L + 3$ STS-VSCRF calculations, respectively.

reaction field potential ($\Delta\phi_{if}^{r} = \Delta\phi_{op}^{(r)}$) corresponding to the electronic relaxation of the solvent ($\epsilon_{op} = 2$ in the solvent region). (5) $\phi_i^r + \Delta\phi_{if}^r$ is then added back to the Hamiltonian of the ADF calculation in step 1. The iteration of steps 1−5 will be repeated until self-consistency between the electron relaxation in the solute and in the solvent is

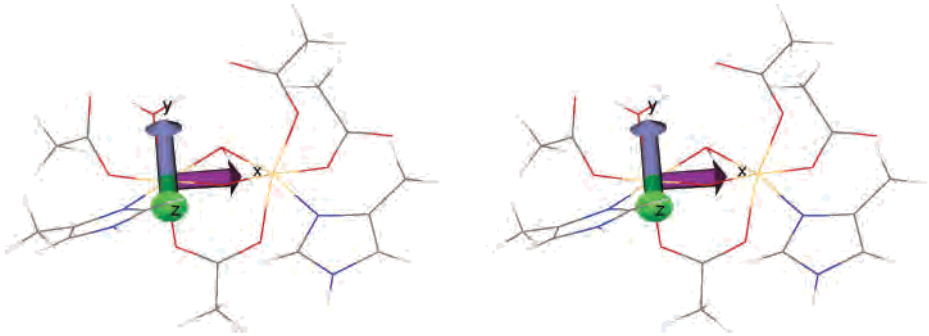

Figure 7. Stereo picture of the diiron center of model II (Y122F) with *xyz* axes.

Table 3. Fe(IV) d−d $n_i \rightarrow n_j = n_L + 3$ Excitation Energies ($\Delta\epsilon_{STS-VSCRF}$, from Equation 2) (eV), Possible Band Numbers, and Fe(IV) d Orbital Populations (%) Obtained from STS-VSCRF Calculations for Model II (Y122F) in a High-Spin AF-Coupled Fe1(III)−Fe2(IV) State

		$n_i \rightarrow n_L + 3$	Fe(IV) d populations	
band	n_i	$\Delta\epsilon_{STS-VSCRF}$	n_i	$n_L + 3$
1	n_H	1.65	$d_{x^2-y^2}$ (16.8), d_{z^2} (10.9), d_{xy} (6.7)	d_{xz} (32.8), $d_{x^2-y^2}$ (3.1), d_{yz} (1.5)
2	$n_H - 4$	2.50	d_{xy} (6.6), d_{yz} (4.8), $d_{x^2-y^2}$ (4.6)	d_{xz} (32.0), $d_{x^2-y^2}$ (2.8), d_{yz} (1.4)
	$n_H - 5$	2.54	d_{xy} (8.3), d_{yz} (3.6), $d_{x^2-y^2}$ (1.5)	d_{xz} (31.4), $d_{x^2-y^2}$ (2.7), d_{yz} (1.4)
3	$n_H - 6$	2.65	d_{z^2} (10.5), $d_{x^2-y^2}$ (4.8)	d_{xz} (31.8), $d_{x^2-y^2}$ (3.1), d_{yz} (1.4)
4	$n_H - 11$	3.15	d_{yz} (9.1), d_{xy} (2.0)	d_{xz} (31.0), $d_{x^2-y^2}$ (3.4), d_{yz} (1.4)
	$n_H - 13$	3.42	d_{yz} (5.7), $d_{x^2-y^2}$ (1.6), d_{xy} (1.4)	d_{xz} (31.4), $d_{x^2-y^2}$ (3.1), d_{yz} (1.4)
	$n_H - 14$	3.48	d_{yz} (2.2)	d_{xz} (31.4), $d_{x^2-y^2}$ (3.1), d_{yz} (1.4)

achieved. Then the vertical excitation energy is computed from eq 3 for the normal one-electron excited-state VSCRF calculation and from eq 2 for the STS-VSCRF calculation.

3. Results and Discussion

As mentioned before, only three low-lying Fe2(IV) d−d transition VSCRF calculations were converged for model I among all one-electron excitation ($n_i \rightarrow n_j$) VSCRF calculations of the four models. These excitation energies obtained from eq 3 are given in Table 1. The main Fe2(IV) d populations (%) in orbitals n_i and n_j are also shown in Table 1. To better understand the *xyz* directions of the atomic orbitals, a stereo picture of the diiron center of model I with *xyz* axes is given in Figure 5. More Fe2(IV) d−d transitions are obtained in the STS-VSCRF calculations for model I (Y122F). The corresponding Fe2(IV) d−d transition energies ($\Delta\epsilon_{STS-VSCRF}$) calculated from eq 2 are given in Table 2 and are compared with the experimental data (ΔE_{exp}).

Amazingly (but consistent with the underlying theory), the first three ($n_i = n_H$, $n_H - 1$, $n_H - 2 \rightarrow n_j = n_L + 3$) Fe(IV) d−d transition energies and the Fe(IV) d populations in n_i and n_j obtained from the STS-VSCRF calculations (Table 2) are almost exactly the same as those obtained from the normal one-electron excitation VSCRF calculations (Table 1). This again demonstrates that the difference of the eigenvalues in STS is a very good approximation for the one-electron excitation energy in DFT.[27]

Molecular orbital plots for the half electrons in the d → d excitation STSs obtained from STS-VSCRF calculations are given in Figure 6. Only one virtual molecular orbital ($n_L + 3$) in model I contains a significant Fe2(IV) d population, and the total contribution of the Fe2(IV) d orbitals to this virtual orbital $n_L + 3$ is as high as 43%. Five low-energy Fe2(IV) d−d STSs ($n_i = n_H$, $n_H - 1$, $n_H - 2$, $n_H - 3$, $n_H - 4 \rightarrow n_L + 3$) for this model were obtained. Their STS energies (energy differences between the orbitals n_i and $n_L + 3$) calculated using eq 2 are 1.95, 2.54, 2.57, 2.89, and 2.71 eV, respectively. The orbital $n_L + 3$ contains strong antibonding character between Fe2(IV) and the bridging oxygen atoms, which push the energy of this orbital up. This orbital therefore represents the empty (the fifth) Fe(IV) d orbital. Orbital n_H also has strong antibonding characteristics between Fe2(IV) and the oxygen atoms in the carboxylate groups. The energy of this orbital is lower than that of $n_L + 3$ but higher than those of other occupied Fe2(IV) d orbitals, which makes n_H the HOMO. The transition states of $n_H - 1 \rightarrow n_L + 3$ and $n_H - 2 \rightarrow n_L + 3$ have very similar transition energies and Fe2(IV) d populations in the corresponding half-occupied orbitals. See Figure 6; the main difference between the two orbitals is that orbital $n_H - 1$ contains some p_y populations (3.0−5.6%) from the carbon atoms of the His241 side chain. The atomic orbital characteristics around the diiron centers are almost the same except that the phases are opposite. These two converged VSCRF calculations should therefore reflect one Fe2(IV) d−d transition state and are therefore grouped as one band (see Table 2). We then actually obtained four Fe(IV) d−d transition states, which are consistent with the electron transitions from the four occupied d orbitals to the one empty d orbital in an Fe(IV) ion. In view of the fact that both the initial and final molecular orbitals of the four numbered excitations have substantial Fe(IV) d population, we expect measurable MCD and optical intensity in these four transitions. A similar argument applies to other models (models II, III, and X_{2nd}). The calculated Fe(IV) d−d transition energies for model I (1.95, {2.54, 2.57}, and {2.71, 2.89} eV) are in very good agreement with the corresponding experimental data (2.07, 2.41, and 2.74 eV).[16]

Previously,[19] we have also estimated the Fe2(IV) d−d transition energies for the model clusters by comparing the

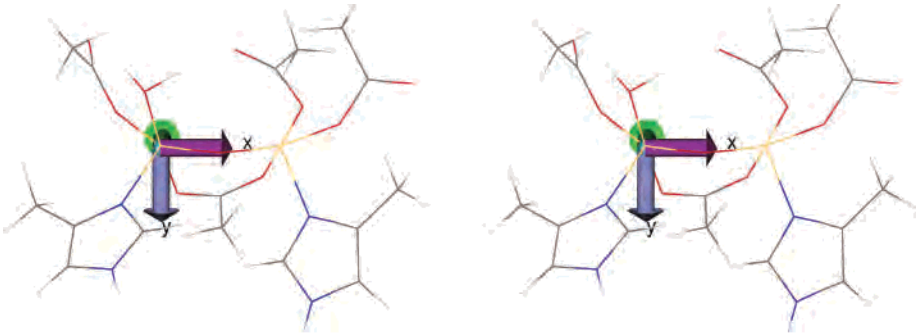

Figure 8. Stereo picture of the diiron center of model III (Y122F) with *xyz* axes.

Table 4. STS-VSCRF-Calculated Fe(IV) d−d $n_i \rightarrow n_j$ ($n_j = n_L + 1$, $n_L + 3$, and $n_L + 4$) Excitation Energies ($\Delta\epsilon_{STS-VSCRF}$) (eV), Possible Band Numbers, and Fe(IV) d Orbital Populations (%) for the High-Spin AF-Coupled Fe1(III)−Fe2(IV) State Model III (Y122F)

	n_i		Fe(IV) d populations	
band	$n_i \rightarrow n_L + 1$	$\Delta\epsilon_{STS-VSCRF}$	n_i	$n_L + 1$
1	n_H	0.55	d_{yz} (18.3), d_{xy} (10.7), d_{xz} (9.0), $d_{x^2-y^2}$ (5.0)	d_{yz} (6.3), d_{xy} (5.9), d_{xz} (1.1)
2	$n_H - 5$	1.37	d_{xy} (9.8), $d_{x^2-y^2}$ (7.5), d_{z^2} (7.5), d_{yz} (7.3), d_{xz} (1.9)	d_{xy} (6.3), d_{yz} (5.7), d_{xz} (1.5)
	$n_H - 6$	1.45	d_{xy} (10.0), $d_{x^2-y^2}$ (7.8), d_{z^2} (7.5), d_{yz} (7.8), d_{xz} (2.1)	d_{xy} (5.5), d_{yz} (5.1), d_{xz} (2.1)
3	$n_H - 7$	1.68	d_{z^2} (9.8), d_{xy} (7.6), d_{yz} (1.1)	d_{yz} (6.7), d_{xy} (5.8), d_{xz} (2.0)
	n_i		Fe(IV) d populations	
band	$n_i \rightarrow n_L + 3$	$\Delta\epsilon_{STS-VSCRF}$	n_i	$n_L + 3$
4	n_H	1.33	d_{yz} (19.1), d_{xy} (11.9), d_{xz} (7.9), $d_{x^2-y^2}$ (4.3)	d_{yz} (7.9), $d_{x^2-y^2}$ (5.7), d_{xz} (4.6), d_{z^2} (3.2)
	$n_H - 1$	1.43	d_{yz} (18.7), d_{xy} (12.2), d_{xz} (6.8), $d_{x^2-y^2}$ (3.8)	d_{yz} (7.3), $d_{x^2-y^2}$ (6.7), d_{xz} (5.4), d_{z^2} (3.5)
5	$n_H - 4$	2.01	d_{xy} (14.9), d_{yz} (9.8), d_{xz} (8.0), d_{z^2} (1.9), $d_{x^2-y^2}$ (1.9)	$d_{x^2-y^2}$ (6.8), d_{yz} (6.4), d_{xz} (5.1), d_{z^2} (3.5)
6	$n_H - 5$	2.01	$d_{x^2-y^2}$ (17.2), d_{xz} (16.3), d_{z^2} (4.2)	$d_{x^2-y^2}$ (7.8), d_{yz} (5.6), d_{xz} (5.2), d_{z^2} (3.7)
7	$n_H - 7$	2.34	d_{z^2} (11.9), $d_{x^2-y^2}$ (4.6), d_{xy} (4.4)	$d_{x^2-y^2}$ (6.9), d_{yz} (6.5), d_{xz} (5.5), d_{z^2} (4.0)
	$n_H - 8$	2.51	d_{z^2} (13.2), $d_{x^2-y^2}$ (3.7)	$d_{x^2-y^2}$ (7.5), d_{xz} (5.9), d_{yz} (5.8), d_{z^2} (3.6)
	n_i		Fe(IV) d populations	
band	$n_i \rightarrow n_L + 4$	$\Delta\epsilon_{STS-VSCRF}$	n_i	$n_L + 4$
8	n_H	1.65	d_{yz} (18.6), d_{xy} (11.8), d_{xz} (7.9), $d_{x^2-y^2}$ (5.7)	$d_{x^2-y^2}$ (6.4), d_{yz} (5.3), d_{xz} (5.0), d_{z^2} (3.0)
9	$n_H - 4$	2.24	$d_{x^2-y^2}$ (28.5), d_{xz} (21.9), d_{z^2} (3.2), d_{yz} (1.8)	$d_{x^2-y^2}$ (5.7), d_{xz} (4.2), d_{yz} (3.1), d_{z^2} (2.3)
	$n_H - 5$	2.35	$d_{x^2-y^2}$ (20.2), d_{xz} (19.9), d_{z^2} (2.0)	$d_{x^2-y^2}$ (5.3), d_{xz} (4.0), d_{yz} (2.2), d_{z^2} (1.9)
10	$n_H - 6$	2.80	d_{z^2} (11.3), d_{xy} (6.4), $d_{x^2-y^2}$ (1.7)	$d_{x^2-y^2}$ (5.0), d_{xz} (4.1), d_{yz} (2.5), d_{z^2} (2.4)
	$n_H - 8$	3.01	d_{z^2} (13.2), $d_{x^2-y^2}$ (1.1), d_{xz} (1.0)	$d_{x^2-y^2}$ (4.7), d_{xz} (3.9), d_{z^2} (2.0), d_{yz} (1.9)

ground-state molecular orbital energy differences between the occupied and virtual orbitals, which contain significant Fe2(IV) d populations (Table 4 in ref 19). The ground-state included COSMO solvation, which will affect both occupied and virtual orbitals. Six low-energy d−d transitions were estimated (only four or five are orbitally distinct) for model I. The transition energies were 1.76, 2.60, 2.77, 2.88, 3.04, and 3.07 eV.[19] Clearly, the current STS-VSCRF method improved the Fe(IV) d−d transition energies by increasing the lowest d−d transition energy and lowering the higher energy d−d bands.

A stereo picture of the diiron center in model II with *xyz* axes is given in Figure 7. Similar to model I, there is also one virtual molecular orbital ($n_L + 3$) in model II, which contains significant Fe2(IV) d populations (up to 37%). Six (see Table 3) low-energy STS-VSCRF converged states ($n_i = n_H$, $n_H - 4$, $n_H - 5$, $n_H - 6$, $n_H - 11$, and $n_H - 13 \rightarrow n_L + 3$) are assigned as Fe2(IV) d−d transitions, in which $n_H - 4$ and $n_H - 5 \rightarrow n_L + 3$ represent the same transition, according to the similar Fe(IV) d and ligand atomic orbital populations. Although the transitions $n_H - 11$ and $n_H - 13 \rightarrow n_L + 3$ are not the same, their main Fe(IV) d characteristics and transition energies are similar. We then grouped these two transitions into one band. Compared with the observed bands, the lowest calculated Fe(IV) d−d transition energy (1.65 eV) for model II is too low and the highest transition energy in the fourth calculated band is too high. Overall, the predicted Fe(IV) d−d transition energies for model II are worse than the corresponding ones for model I compared with experiment.

The diiron center of model III with *xyz* axes is shown in Figure 8. The calculation for the Fe(IV) d−d transitions in model III is complicated and difficult to analyze (see Table 4). Not only the virtual orbital $n_L + 3$ but also $n_L + 1$ and $n_L + 4$ of this model contain the Fe2(IV) d populations, each with a much smaller percentage than in the $n_L + 3$ orbitals of models I and II. Therefore, for each relevant occupied orbital, we performed three STS-VSCRF calculations of $n_i \rightarrow n_L + 1$, $n_L + 3$, and $n_L + 4$. Unlike the STS-VSCRF calculations for models I and II, most of the SCF processes in the transition-state calculations for model III are difficult to converge. We had to lower the SCF convergence criterion from 1×10^{-4} to 1×10^{-3} or 0.005. Testing calculations for model I show that if the transition state can be reached with the SCF convergence criterion of 1×10^{-4}, lowering the criterion to 1×10^{-3} or even 0.005 produces essentially

Table 5. STS-VSCRF-Calculated Fe(IV) d−d $n_i \rightarrow n_j$ ($n_j = n_L$ and $n_L + 3$) Excitation Energies ($\Delta\epsilon_{STS-VSCRF}$) (eV), Possible Band Numbers, and Fe(IV) d Orbital Populations (%) for Model X_{2nd} (Figure 4) in a High-Spin AF-Coupled Fe1(III)−Fe2(IV) State

band	$n_i \rightarrow n_L$	$\Delta\epsilon_{STS-VSCRF}$	Fe(IV) d populations n_i	Fe(IV) d populations n_L
1	$n_H - 1$	0.56	d_{xy} (13.4), $d_{x^2-y^2}$ (11.9), d_{z^2} (9.2), d_{yz} (1.5)	d_{xz} (8.4), d_{yz} (1.4), d_{z^2} (1.1)
2	$n_H - 5$	1.51	d_{xy} (4.1), $d_{x^2-y^2}$ (3.9), d_{yz} (1.1)	d_{xz} (11.4), d_{yz} (1.7), d_{z^2} (1.3)
	$n_H - 6$	1.63	d_{xy} (8.0), $d_{x^2-y^2}$ (6.3), d_{yz} (5.8)	d_{xz} (9.8), d_{yz} (1.7), d_{z^2} (1.4)
3	$n_H - 7$	1.77	d_{z^2} (13.2), d_{yz} (7.3), $d_{x^2-y^2}$ (2.2)	d_{xz} (9.6), d_{yz} (1.8), d_{z^2} (1.3)
	$n_H - 8$	1.84	d_{z^2} (16.5), d_{xy} (6.5), d_{xz} (1.9)	d_{xz} (10.1), d_{yz} (1.7), d_{z^2} (1.3)
4	$n_H - 16$	2.71	d_{z^2} (6.3), $d_{x^2-y^2}$ (3.5), d_{xz} (1.1)	d_{xz} (9.6), d_{yz} (1.6), d_{z^2} (1.1)
5	$n_H - 17$	2.85	d_{yz} (6.3), $d_{x^2-y^2}$ (4.4)	d_{xz} (11.2), d_{yz} (1.6), d_{z^2} (1.1)

band	$n_i \rightarrow n_L + 3$	$\Delta\epsilon_{STS-VSCRF}$	Fe(IV) d populations n_i	Fe(IV) d populations $n_L + 3$
6	n_H	1.48	d_{xy} (12.3), $d_{x^2-y^2}$ (11.2), d_{z^2} (8.9), d_{yz} (1.5)	d_{xz} (17.9), $d_{x^2-y^2}$ (4.9), d_{xz} (1.2), d_{z^2} (1.1)
7	$n_H - 5$	2.33	d_{xy} (4.2), $d_{x^2-y^2}$ (3.6), d_{yz} (1.3)	d_{xz} (16.4), $d_{x^2-y^2}$ (4.8), d_{xz} (1.2)
8	$n_H - 7$	2.71	d_{yz} (7.2), d_{z^2} (7.0), $d_{x^2-y^2}$ (1.4)	d_{xz} (16.9), $d_{x^2-y^2}$ (5.1), d_{xz} (1.2)
9	$n_H - 8$	2.73	d_{z^2} (15.3), d_{xy} (3.8), d_{xz} (1.6), d_{yz} (1.5)	d_{xz} (17.3), $d_{x^2-y^2}$ (5.1), d_{xz} (1.2)
	$n_H - 9$	2.76	d_{z^2} (9.4), d_{xz} (3.7), $d_{x^2-y^2}$ (2.1)	d_{xz} (17.0), $d_{x^2-y^2}$ (4.8), d_{xz} (1.3)
10	$n_H - 15$	3.43	$d_{x^2-y^2}$ (6.7), d_{xz} (5.3), d_{z^2} (2.5)	d_{xz} (17.3), $d_{x^2-y^2}$ (5.1), d_{xz} (1.2)

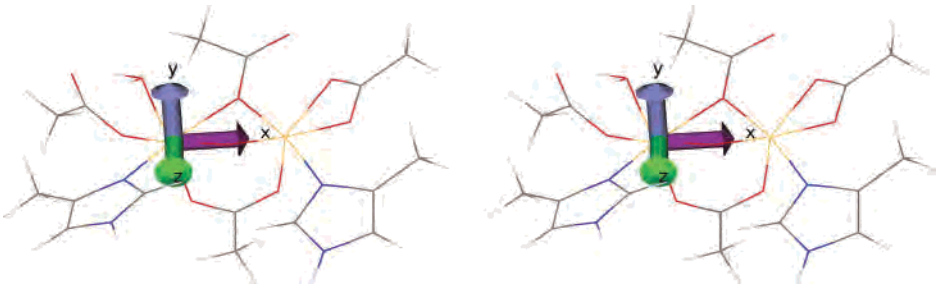

Figure 9. Stereo picture of the diiron center of model X_{2nd} (Y122F) with *xyz* axes.

the same transition energies and Fe(IV) d populations in the initial and final molecular orbitals. However, it is hard to predict the errors for the calculations that can only be converged with the SCF convergence criterion of 0.005. The relative energies of the molecular orbitals may converge well with the low SCF convergence. The Fe(IV) d populations for the initial and final orbitals may not be as accurate. The Fe2(IV) d−d transition energies and the possible band numbers obtained for model III are given in Table 4. Even if we ignore all of the $n_i \rightarrow n_L + 1$ transitions (because the Fe(IV) d populations in orbital $n_L + 1$ are relatively lower than those in $n_L + 3$ and $n_L + 4$), there are still about seven calculated Fe(IV) d−d transition bands for model III. If this model does represent the active site of RNR-X, the MCD experiment should show more than three bands for Fe(IV) d−d transitions because the transitions with similar energies but different Fe(IV) d characteristics should be distinctive in MCD spectra (with positive and negative peaks). Aside from the complexity of these Fe2(IV) d−d transitions of this model, the excitation energies of the lower-energy bands are too low compared with experiment. Overall, the calculated Fe(IV) d−d transition energies for model III are much worse than those predicted for model I.

The STS-VSCRF results for model X_{2nd} (Figure 4) are given in Table 5. Note that the molecular orientation of this smaller cluster is different from that of the large one studied in refs 18 and 19. A stereo picture of the diiron center of the current X_{2nd} cluster is shown in Figure 9. Similar to model III, more than one of the virtual orbitals of X_{2nd} (orbitals n_L and $n_L + 3$) contain significant Fe(IV) d populations. Orbital $n_L + 3$ has more Fe(IV) d contribution than n_L. Therefore, the transitions of $n_i \rightarrow n_L + 3$ are more important than those of $n_i \rightarrow n_L$. However, the transitions can still be mixed together and make the spectra complicated. Some of the STS-VSCRF calculations for X_{2nd} also had a SCF convergence problem, and we had to lower the SCF convergence criteria from 1×10^{-4} to 1×10^{-3}. Even if we ignore the transitions of $n_i \rightarrow n_L$, bands 1−5 (using a rationale similar to that of the model III discussion), there will be five calculated Fe(IV) d−d transition bands left for this model. The first transition energy (1.48 eV) is too low compared with the observed energy (2.07 eV), similar to the corresponding results for models II and III, and the last transition energy (3.43 eV, band 10) is significantly too high compared to experiment (2.74 eV).

4. Conclusions

In this paper, we have presented the calculated Fe(IV) d−d transition energies for four active-site structure models of class I RNR intermediate X, using the broken-symmetry DFT STS-VSCRF methodology. The predicted Fe(IV) d−d transition energies for model I (in Y122F form and in the AF-coupled Fe1(III)−Fe2(IV) state with high-spin sites) are the best in comparison with the corresponding experimentally observed low-energy Fe(IV) d−d transition bands for X in the double-mutant Y122F/Y356 RNR-R2. Other properties of these model clusters studied in ref 19 in both the wild-type and mutant Y122F forms, including geometries, ener-

gies, spin states, pK_a's, ^{57}Fe, ^{1}H, and ^{17}O hyperfine tensors, and ^{57}Fe Mössbauer isomer shifts and quadrupole splittings, also indicate that model I, which contains two μ-oxo bridges and a terminal water (bound to Fe1) in the high-spin AF-coupled Fe1(III)−Fe2(IV) state, is the best in reproducing most of the observed properties of RNR-X. Our current Fe(IV) d−d transition calculations further support the proposal that model I represents the active-site structure of class I RNR intermediate X well.

Acknowledgment. We thank the NIH for financial support (Grant GM43278 to L.N.). The generous support of computer resources of the Scripps Research Institute is gratefully acknowledged. We thank Laura Hunsicker-Wang, Martin Bollinger, Edward Solomon, and Brian Hoffman for valuable discussions on spectroscopy.

Supporting Information Available: The Cartesian coordinates of our COSMO-optimized geometries of the Fe1(III)Fe2(IV) state Y122F form models I−III and X_{2nd}. This material is available free of charge via the Internet at http://pubs.acs.org.

IC060566+